Acta Mech 229, 849–866 (2018)
https://doi.org/10.1007/s00707-017-2004-3

ORIGINAL PAPER

Johannes Kalliauer · Thomas Schlappal · Markus Vill · Herbert Mang · Bernhard Pichler

Bearing capacity of concrete hinges subjected to eccentric compression: multiscale structural analysis of experiments

This paper is dedicated to the memory of Franz Ziegler

Received: 24 March 2017 / Revised: 11 June 2017 / Published online: 17 January 2018

Abstract Existing design guidelines for concrete hinges are focusing on serviceability limit states. Lack of knowledge about ultimate limit states was the motivation for this work. Experimental data are taken from a testing series on reinforced concrete hinges subjected to eccentric compression up to their bearing capacity. These tests are simulated using the finite element (FE) software Atena science and a material model for concrete implemented therein. The first simulation is based on default input derived from measured values of Young's modulus and of the cube compressive strength of the concrete. The numerical results overestimate the initial stiffness and the bearing capacity of the tested concrete hinges. Therefore, it is concluded that concrete was damaged already before the tests. A multiscale model for tensile failure of concrete is used to correlate the preexisting damage to corresponding values of Young's modulus, the tensile strength, and the fracture energy of concrete. This allows for identifying the preexisting damage in the context of correlated structural sensitivity analyses, such that the simulated initial stiffness agrees well with experimental data. In order to simulate the bearing capacity adequately, the triaxial compressive strength of concrete is reduced to a level that is consistent with regulations according to Eurocode 2. Corresponding FE simulations suggest that the ductile *structural* failure of concrete hinges results from the ductile *material* failure of concrete at the surface of the compressed lateral notch. Finally, Eurocode-inspired interaction envelopes for concrete hinges subjected to compression and bending are derived. They agree well with the experimental data.

List of symbols

a	Neck width
a_g	Maximum aggregate size
b_1	Width of the partially loaded area A_{c0}
b_2	Width of the partially loaded area A_{c1}
c	Softening parameter
c_1, c_2	Coefficients appearing in the crack opening law

J. Kalliauer · T. Schlappal · H. Mang · B. Pichler (✉)
Institute for Mechanics of Materials and Structures, TU Wien – Vienna University of Technology,
Karlsplatz 13/202, 1040 Vienna, Austria
E-mail: Bernhard.Pichler@tuwien.ac.at
Tel.: +43-58801-20224
Fax: +43-588019-20224

M. Vill
Vill Ziviltechniker GmbH, Hermanngasse 18, 1070 Vienna, Austria

H. Mang
College of Civil Engineering, Tongji University, Siping Road 1239, Shanghai 200092, China

c_{ini}	Initial value of c
d_1	Depth of the partially loaded area A_{c0}
d_2	Depth of the partially loaded area A_{c1}
e	Eccentricity of the normal force
e_σ	Parameter influencing the Menétrey–Willam failure surface in the deviatoric plane
$\boldsymbol{e}_x$, $\boldsymbol{e}_y$, $\boldsymbol{e}_z$	base vectors in x, y, and z-direction
f_c	Uniaxial compressive strength
f_{c0}	Initial elastic limit under uniaxial compression
f_c'	Evolving elastic limit under uniaxial compression
f_{cd}	Design value of the uniaxial compressive strength
f_{ck}	Characteristic value of the uniaxial compressive strength
$f_{c,\mathrm{cube}}$	Mean value of the cube compressive strength
$f_{ck,\mathrm{cube}}$	Characteristic value of the cube compressive strength
f_t	Uniaxial tensile strength of the Rankine failure surface
f_t'	Uniaxial tensile strength of the Menétrey–Willam failure surface
$f_{t,\mathrm{dam}}$	Uniaxial tensile strength of damaged concrete
m	Parameter influencing the shape of the Menétrey–Willam failure surface
r_c	Reduction of uniaxial compressive strength, due to cracks with crack-plane normal vectors orthogonal to the loading direction
w	Crack opening displacement
w_c	Value of w corresponding to the vanishing cohesive stress
w_d	Critical compression displacement
w_{dam}	Value of w due to preexisting damage
x, y, z	Cartesian coordinates
A_{c0}	Partially loaded area
A_{c1}	Distribution area with a similar shape to A_{c0}
E	Young's modulus
E_c	Young's modulus of uncracked concrete
$E_{c,\mathrm{dam}}$	Young's modulus of damaged concrete
F_{3P}^p	Failure function of the Menétrey and Willam criterion
F_{Rdu}	Maximum design compressive force
$Fixed$	Flag for modeling of crack rotation: $Fixed = 1$ … no crack rotation
G_f	Fracture energy
$G_{f,\mathrm{dam}}$	Fracture energy of damaged concrete
K_{Ic}	Fracture toughness
M	Bending moment
N	Normal force
β	Flag for modeling the direction of the plastic flow: $\beta = 0$ … purely deviatoric plastic flow
ΔG_f	Reduction of fracture energy due to preexisting damage
$\Delta\varphi$	Rotation angle
ϵ_c^p	Plastic strain at uniaxial compressive strength
ϑ	Lode angle
λ_t	Auxiliary-to-actual uniaxial tensile strength ratio
ν	Poisson's ratio
ν_c	Poisson's ratio of uncracked concrete
ξ	Hydrostatic stress invariant
ρ	Deviatoric stress invariant
σ	Softening tensile strength of smeared crack model
$\boldsymbol{\sigma}$	Cauchy stress tensor
σ_1, σ_2, σ_3	Principal stresses
σ_ℓ	Principal normal stress in the loading direction
$\sigma_{\ell u}$	Maximum normal stress in the loading direction
σ_y	von Mises yield stress of steel
ω	Crack density parameter

1 Introduction

Concrete hinges were invented by Freyssinet [13,14]. They are unreinforced or marginally reinforced necks in reinforced concrete structures [30,37]. In practical engineering, they are used as supports in bridge construction [30,34,36–38] and as segment-to-segment interfaces of segmented linings used in mechanized tunneling [3,11,21,22,28]. In the latter context, concrete hinges are one of the main challenges for finite element (FE) simulations of segmented tunnels [10,18,24,29,40,42]. Eventually, a few pairs of crossed steel rebars (or bolts) run across a concrete hinge. Their crossover point is typically at the center of the neck. Therefore, the bending stiffness of the neck is significantly smaller than that of the two connected reinforced concrete parts. The corresponding concentration of bending deformations at the concrete hinge results—already under regular service loads—in tension-induced cracking of initially monolithic necks [26,27,30–32], or in partial separation of segment-to-segment interfaces [16,21]. Both effects reduce the bending stiffness of the neck. This increases the rotational compliance of concrete hinges, characterized by large, concentrated rotations of cross sections.

Pioneering design guidelines for concrete hinges were developed by Leonhardt and Reimann [27]. They refer to the deterministic safety concept used in the 1960s. Given that nowadays a semi-probabilistic safety concept is used, Marx [30] translated the guidelines by Leonhardt and Reimann into the nomenclature of modern European design standards. The latter require consideration of both serviceability limit states (SLS) and ultimate limit states (ULS). Notably, the guidelines by Leonhardt and Reimann focus rather on the SLS. This has provided the motivation for the present contribution. It is devoted to the structural re-analysis of a test series regarding the bearing capacity of concrete hinges, subjected to eccentric compression [39].

The aims of the present contribution are (1) to identify the mechanisms which render failure of concrete hinges in a very ductile fashion possible, and (2) to check whether or not a Eurocode-inspired failure envelope can provide reasonable estimates of the bearing capacity of concrete hinges subjected to compression and bending. As for the first aim, nonlinear FE simulations are carried out with the software Atena science and a material model for concrete implemented therein [8]. Two-dimensional plane strain simulations and three-dimensional simulations are carried out in order to gain insight into (1) the triaxiality of compressive stress states in the neck region, and (2) the structural behavior of concrete hinges under eccentric compression right up to the their bearing capacity. As for the second aim, Eurocode regulations for partially loaded areas [4] are the starting point for the derivation of failure envelopes for concrete hinges subjected to compression and bending.

In the context of reproducing experimental measurements by means of three-dimensional FE analyses, the number of fitting parameters required is kept as small as possible. This is accomplished by combining the *structural* FE model with a recently developed multiscale *material* model for tensile failure of concrete [19]. The micromechanics-based model considers interacting cracks as microstructural entities of concrete. As the damage variable, the Budiansky and O'Connell crack density parameter is used [5]. The described combination of models allows for correlated structural sensitivity analyses. Input values of Young's modulus, the tensile strength, and the fracture energy of concrete are prescribed such that they refer to one and only one value of the crack density. This reduces the number of fitting parameters from three to one and results in a multiscale structural analysis of concrete hinges.

The manuscript is structured as follows. In Sect. 2 experimental data on concrete hinges subjected to eccentric compression are summarized. Section 3 is devoted to nonlinear FE simulations of concrete hinges, carried out in the framework of multiscale structural analysis. Section 4 deals with the derivation of failure envelopes for concrete hinges subjected to compression and bending. Section 5 contains discussions of the obtained results. Conclusions of the present study are presented in Sect. 6.

2 Experimental data from testing of concrete hinges, taken from [39]

The tested reinforced concrete hinges consisted of concrete that was produced with a commercial CEM II/A-L 42.5 N cement, Viennese tab water, and calcite aggregates exhibiting a maximum size of 16 mm. The initial water-to-cement and aggregate-to-cement mass ratios amounted to 0.48 and 3.97, respectively. The cube compressive strength, $f_{c,\mathrm{cube}}$, and Young's modulus, E, were determined 28 days after production, following the Austrian standards for testing of concrete [1]. The mean values of two tests ($f_{c,\mathrm{cube},1} = 55\,\mathrm{MPa}$, $E_1 = 34.3\,\mathrm{GPa}$; $f_{c,\mathrm{cube},2} = 57.5\,\mathrm{MPa}$, $E_2 = 35.2\,\mathrm{GPa}$) read as [39]

$$f_{c,\mathrm{cube}} = 56.25\,\mathrm{MPa}, \qquad E = 34.75\,\mathrm{GPa}. \tag{1}$$

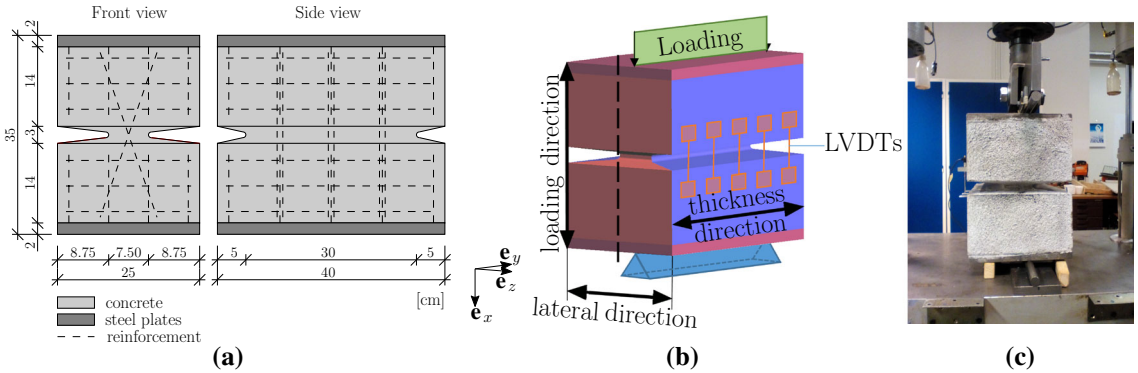

Fig. 1 Concrete hinges tested in [39]: **a** geometric dimensions and arrangement of the steel reinforcement, **b** definition of the Cartesian coordinate system: x denotes the loading direction, y the thickness direction, and z the lateral direction; schematic illustration of the loading and the support conditions as well as of the positions of the displacement sensors (LVDTs), and **c** photo of the test setup: the timber bars were removed during testing

The steel quality of the rebars was chosen as B550 A. The expected value of the von Mises yield stress of this steel amounts to 605 MPa.

The geometric shape of the tested concrete hinges complied with the design guidelines of Leonhardt and Reimann [27]. The overall width amounted to 25 cm, the height to 35 cm, and the depth to 40 cm, see Fig. 1a. The depth of the lateral and the front-side notches amounted to 8.75 and 5 cm, respectively. Therefore, the cross section of the neck was equal to $7.5 \times 30\,\text{cm}^2$, see Fig. 1a. At the top and the bottom of the concrete hinges, steel plates of two centimeter thickness were provided. They ensured an effective distribution of the concentrated external line loads. Each steel plate was welded to the neighboring reinforcement cage. The top and bottom reinforcement cages, in turn, were connected by three pairs of crossed steel rebars, with crossover points right at the center of the neck, see Fig. 1a.

During testing, three nominally identically concrete hinges were subjected, one after another, to eccentric line loads, see Fig. 1b. This resulted in combined compression and bending, whereby the bending moment M was equal to the applied normal force N times the eccentricity e:

$$M = N\,e. \tag{2}$$

As for the quantification of the displacements, inductive displacement sensors (LVDTs) were mounted at the lateral surfaces of the concrete hinges. They permitted measuring changes of the notch mouth opening displacements of the lateral notches. Thus, they allowed for quantifying the rotation angles [39].

In order to characterize the undamaged bending stiffness of the neck region, compression tests were carried out with an eccentricity $e = 20\,\text{mm}$. This value was chosen such that no significant bending-induced tensile cracking was induced when increasing the normal force up to 200 kN [39]. The tests on all three concrete hinges delivered very similar results, see Fig. 2a. Hence, the tests satisfy the criterion of repeatability in a very satisfactory manner. The measured force–rotation relationships are virtually linear. The rotation angle of the neck at 200 kN amounted to some 0.75 mrad, see Fig. 2a.

In order to determine the bearing capacity of the concrete hinges, compression tests were carried out with an eccentricity of $e = 25\,\text{mm}$. This value was chosen to be equal to one-third of the neck width, given as

$$a = 75\,\text{mm}, \tag{3}$$

because the ratio $e/a = 1/3$ refers to the limit of applicability of the design guidelines of Leonhardt and Reimann [27]. Accordingly, the bending-induced tensile crack is expected to propagate across half of the neck width. The tests on all three concrete hinges delivered very similar results, see Fig. 2b. This underlines a very satisfactory test repeatability. Once the normal force exceeded 200 kN, the rotation angles increased superlinearly with increasing loading. When the rotation angles exceeded 15 mrad, the loading could no longer be increased significantly. The bearing capacity of all three tested concrete hinges was equal to approximately 700 kN. This is related to a bending moment which is equal to approximately 17.5 kNm, see Eq. (2) and consider $e = 25\,\text{mm}$.

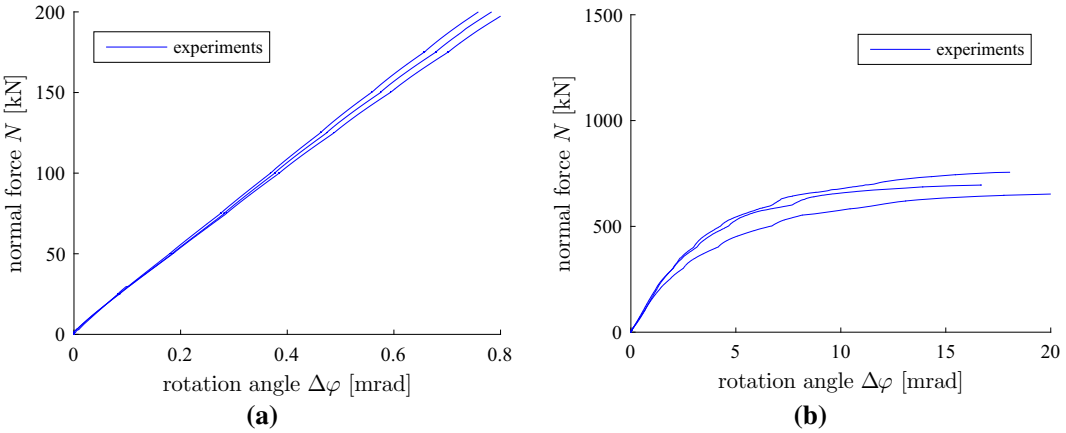

Fig. 2 Measured relations between the eccentric normal force N and the rotation angle $\Delta\varphi$ of three nominally identical concrete hinges: **a** eccentricity $e = 20$ mm, and **b** eccentricity $e = 25$ mm; experimental data from [39]

3 FE simulations of the tested concrete hinges

Geometrically linear FE simulations are performed with version 5.1 of Atena science [8]. The FE simulations are based on expected values of all material properties.

Inelastic material behavior of concrete is modeled based on two failure surfaces: (1) a Rankine surface for the description of tension-induced failure, and (2) a Menétrey–Willam failure surface [7,8,33] for compression-induced failure. The latter is a function of the hydrostatic stress invariant, ξ, the deviatoric stress invariant, ρ, and the Lode angle, ϑ. It reads as

$$F_{3P}^{p}(\xi, \rho, \vartheta) = \frac{3}{2}\left(\frac{\rho}{f_c'}\right)^2 + \frac{m}{f_c'}\left(\rho\,\frac{r(\vartheta)}{\sqrt{6}} + \frac{\xi}{\sqrt{3}}\right) - c \le 0, \tag{4}$$

where m and $r(\vartheta)$, respectively, are defined as

$$m = \frac{3\,e_\sigma}{e_\sigma + 1}\,\frac{f_c'^2 - f_t'^2}{f_c'\,f_t'}, \tag{5}$$

and

$$r(\vartheta) = \frac{4\,(1 - e_\sigma^2)\,\cos^2\vartheta + (2\,e_\sigma - 1)^2}{2\,(1 - e_\sigma^2)\,\cos\vartheta + (2\,e_\sigma - 1)\,\sqrt{4\,(1 - e_\sigma^2)\,\cos^2\vartheta + 5\,e_\sigma^2 - 4\,e_\sigma}}. \tag{6}$$

In Eqs. (4)–(6), c denotes the hardening/softening parameter [8], with an initial value $c_{ini} = 1$, e_σ stands for the so-called eccentricity of the failure surface in deviatoric planes, with a default value $e_\sigma = 0.52$, and f_c' denotes the evolving elastic limit stress of concrete under uniaxial compression. Notably, because of strain hardening f_c' is allowed to increase from its initial value, f_{c0}, up to the uniaxial compressive strength, f_c. Both f_{c0} and f_c are input values for the material model. The symbol f_t' denotes the *auxiliary* uniaxial tensile strength predicted by the Menétrey–Willam failure surface, while the *actual* uniaxial tensile strength, f_t, with $f_t < f_t'$, refers to the Rankine criterion. Notably, the definitions of ξ, ρ, and ϑ for a principle stress state $\boldsymbol{\sigma} = \sigma_1\,\mathbf{e}_x \otimes \mathbf{e}_x + \sigma_2\,\mathbf{e}_y \otimes \mathbf{e}_y + \sigma_3\,\mathbf{e}_z \otimes \mathbf{e}_z$ read as [17,33]

$$\xi = \frac{\sigma_1 + \sigma_2 + \sigma_3}{\sqrt{3}}, \tag{7}$$

$$\rho = \sqrt{\frac{1}{3}\left[(\sigma_1 - \sigma_2)^2 + (\sigma_2 - \sigma_3)^2 + (\sigma_3 - \sigma_1)^2\right]}, \tag{8}$$

$$\vartheta = \frac{1}{3}\,\arccos\left(\frac{(\sigma_1 + \sigma_2 - 2\sigma_3)(2\sigma_1 - \sigma_2 - \sigma_3)(\sigma_1 - 2\sigma_2 + \sigma_3)}{2\left[\sigma_1^2 - \sigma_1\,(\sigma_2 + \sigma_3) + \sigma_2^2 - \sigma_2\,\sigma_3 + \sigma_3^2\right]^{3/2}}\right). \tag{9}$$

Table 1 Default input values for the concrete model "CC3DNonLinCementitious2" of Atena science, related to the cube compressive strength and to Young's modulus according to Eq. (1) and to the maximum aggregate size amounting to 0.016 m

Young's modulus	E	34,750 MPa
Poisson's ratio	ν	0.2
Uniaxial tensile strength	f_t	3.57 MPa
Uniaxial compressive strength	f_c	49 MPa
Fracture energy	G_f	147 J/m^2
Critical compression displacement	w_d	0.5 mm
Eccentricity of the Menétrey–Willam failure surface	e_σ	0.52
Direction of plastic flow ($\beta = 0 \ldots$ purely deviatoric plastic strains)	β	0
Elastic limit for uniaxial compression	f_{c0}	7.49 MPa
Plastic strain at uniaxial compressive strength	ϵ_c^p	1.24×10^{-3}
Control of crack rotation ($Fixed = 1 \ldots$ no crack rotation)	$Fixed$	1
Compressive strength reduction from cracks orthogonal to the loading direction	r_c	0.8
Maximum aggregate size	a_g	0.016 m
Auxiliary-to-actual uniaxial tensile strength ratio	λ_t	2

3.1 Default input values related to the measured stiffness and strength of concrete

The material model employed for concrete requires 14 numerical input values, see Table 1. The only mandatory input is the uniaxial compressive strength. Depending on the corresponding prescribed value, the available software suggests correlated default values for all other input values.

As for the analyzed concrete hinges, the uniaxial compressive strength of concrete can be quantified based on the determined mean cube compressive strength, see Eq. (1), and on the following standard relations [4]:

$$\begin{aligned} f_{ck,\text{cube}} &= f_{c,\text{cube}} - 8\,\text{MPa} = 48.25\,\text{MPa}, \\ f_{ck} &= 0.85\, f_{ck,\text{cube}} = 41\,\text{MPa}, \\ f_c &= f_{ck} + 8\,\text{MPa} = 49\,\text{MPa}, \end{aligned} \tag{10}$$

where the index k denotes *characteristic* strength values, i.e., strength values for semi-probabilistic design calculations.

The standard relation between the uniaxial compressive strength and the uniaxial tensile strength reads as [4,12]

$$f_t = 0.30\, f_{ck}^{2/3}, \tag{11}$$

where both strength values need to be inserted in MPa [4,12]. Evaluating Eq. (11) for f_{ck} according to Eq. (10) delivers $f_t = 3.57$ MPa, see also Table 1.

The relation between the uniaxial compressive strength and Young's modulus according to the Model Code 2010 [12] and the implemented GiD-user-Interface from Atena [9] reads as

$$E = 21{,}500 \left(\frac{f_{ck} + 8}{10} \right)^{\frac{1}{3}}, \tag{12}$$

where E and f_{ck} need to be inserted in MPa [9,12]. Evaluating Eq. (12) for f_{ck} according to Eq. (10) delivers $E = 36{,}521$ MPa. This default value is by 5% larger than the stiffness value identified by means of material characterization, see Eq. (1). For the sake of maximizing the reliability of the FE simulations, the default value is replaced by the "measured" value. The other input variables remain the same as before. This underlines the fact that the used software considers default input values to be *statistically uncorrelated*, except for the initially mentioned correlation between the uniaxial compressive strength and the other default input values.

3.2 Quantification of the stress triaxiality in the neck region

In order to gain insight into the triaxiality of the compressive stresses in the neck region, two-dimensional plane strain FE simulations were carried out. The FE mesh consisted of 26,400 quadrilateral finite elements with bilinear displacement interpolation, 26,885 nodes, and 53,770 degrees of freedom, see Fig. 3a for an illustration of one quarter of the mesh. This discretization was the result of a mesh sensitivity investigation [23].

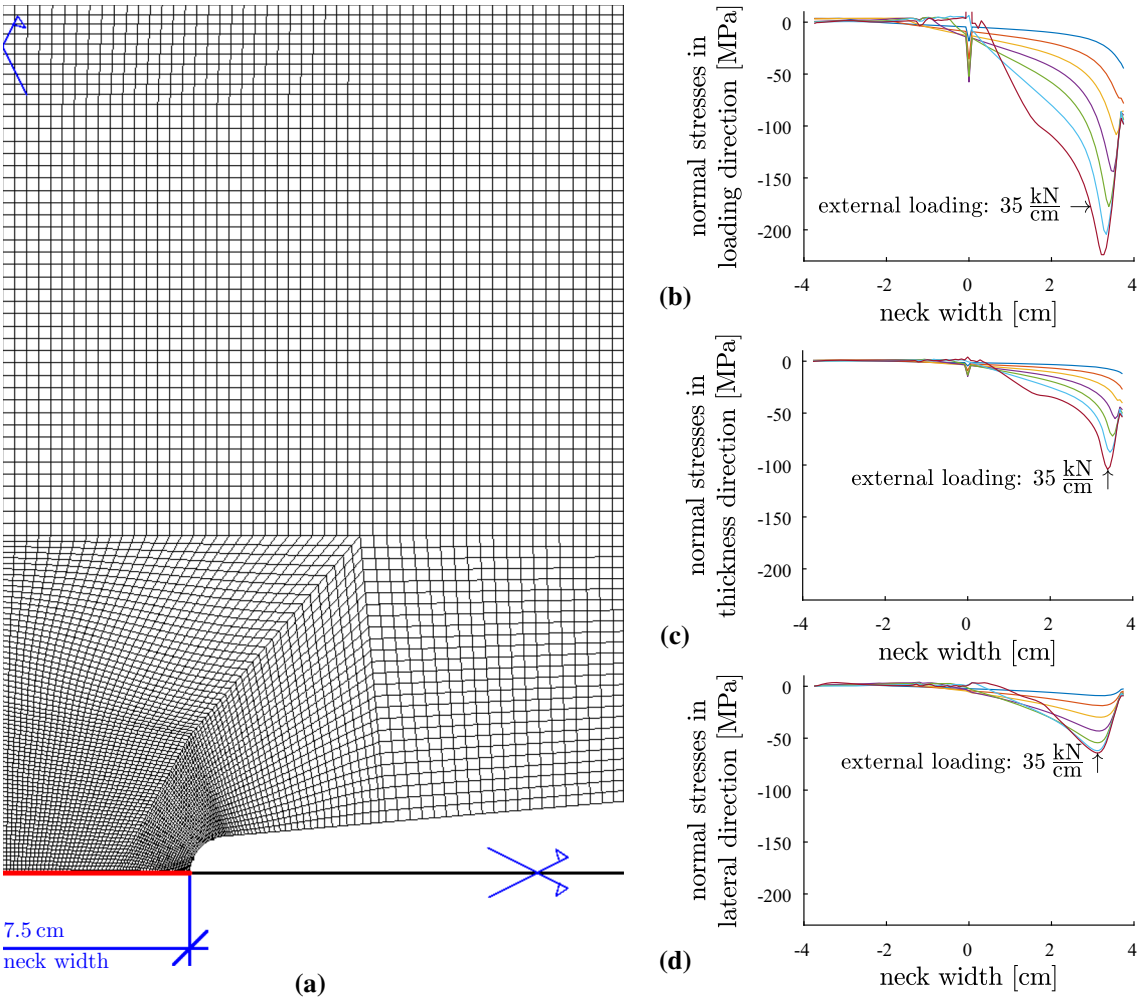

Fig. 3 Two-dimensional plane strain FE simulations of concrete hinges: **a** one quarter of the used FE mesh, consisting of 26,400 quadrilateral finite elements with bilinear displacement interpolation, 26,885 nodes, and 53,770 degrees of freedom, and **b–d** principal compressive normal stresses (in the loading, the thickness, and the lateral direction, respectively) across the neck width, computed with input values listed in Table 1: the seven graphs refer to external load intensities, increased in steps of 5 kN/cm; discontinuities of the stress distributions around $z = 0$ result from the smeared consideration of the reinforcement bars

With increasing fineness of the mesh, the difference of the results for different meshes was decreasing. The used mesh represents a close-to-optimal trade-off between simulation effort and reliability of the numerical results.

By analogy to the bearing capacity tests, compression with an eccentricity $e = 25$ mm was simulated. Input values were taken from Table 1. In the context of an incremental-iterative solution scheme, the loading was increased in increments of 0.5 kN/cm, such that a simulated load of 35 kN/cm was reached after 70 increments. The stress distributions were evaluated along the neck width, see the red line in Fig. 3a. Principal stress states prevail along this line, because it coincides with the intersection of two planes of symmetry of the simulated concrete hinge, see Figs. 3b–d for the distributions of the principal stresses acting in the loading direction, the lateral direction, and in the thickness direction, respectively. Notably, the discontinuities of the stress distributions around $z = 0$, see Figs. 3b–d, result from the smeared consideration of the reinforcement bars [8].

Relatively large compressive stresses are limited to one half of the neck width, see Figs. 3b–d. This is consistent with the design guidelines of Leonhardt and Reimann [27], which suggest that the bending-induced tensile crack propagates across half of the neck width, provided that $e/a = 1/3$, as in the simulated case. The compressive stresses increase with increasing distance from the center of the concrete hinge, they reach a maximum close to the lateral surface, and they decrease sharply in the immediate vicinity of the free lateral surface. Normal stresses in the lateral direction even vanish at the free surface of the neck, see Fig. 3d, because of the

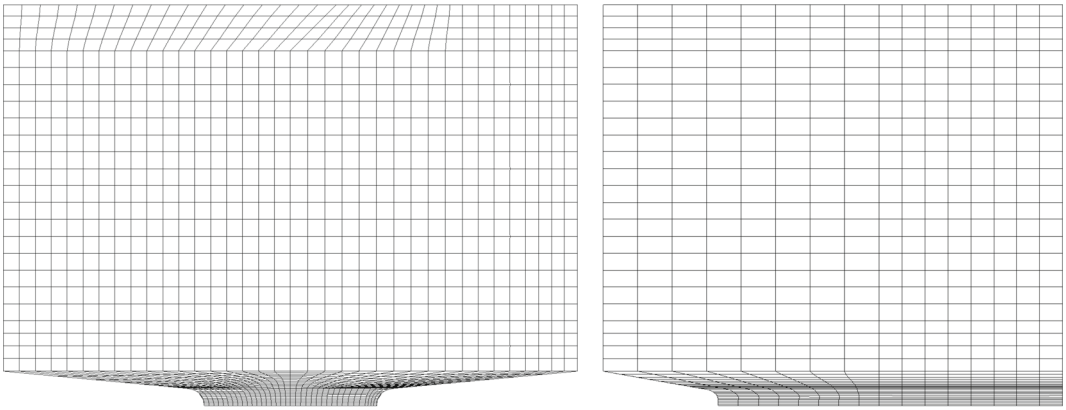

Fig. 4 Three-dimensional FE mesh of one-fourth of the investigated concrete hinges: the mesh consists of 27776 hexahedral finite elements with trilinear displacement interpolation, 31730 nodes, and 95190 degrees of freedom. **a** Thickness direction, **b** lateral direction

traction-free boundary condition prevailing there. At an external load intensity of 35 kN/cm, the distribution of the compressive stresses, acting in the loading direction, is somewhat reminiscent of a *triangular* distribution, see Fig. 3a, such as considered by the design guidelines of Leonhardt and Reimann [27]. The largest compressive normal stresses, obtained for an external load intensity of 35 kN/cm, amount to 224, 104, and 64 MPa, in the loading direction, the thickness direction, and in the lateral direction, respectively, see Figs. 3b–d. This underlines that concrete is subjected to significant triaxial compression in the neck region. The characteristic principal stress ratios amount to 1.00 : 0.45 : 0.30, and the characteristic triaxial compressive stress state $\boldsymbol{\sigma}$ reads as

$$\boldsymbol{\sigma} = \sigma_\ell \cdot \left[1.00\,\mathbf{e}_x \otimes \mathbf{e}_x + 0.45\,\mathbf{e}_y \otimes \mathbf{e}_y + 0.30\,\mathbf{e}_z \otimes \mathbf{e}_z\right], \tag{13}$$

where σ_ℓ denotes the principal compressive normal stress in the loading direction. The isotropic ("hydrostatic") part of the stress state amounts to almost 60% of σ_ℓ. This confinement results in a significant strengthening of concrete, relative to its uniaxial compressive strength.

3.3 Three-dimensional FE simulations of eccentric compression tests

As for three-dimensional FE simulations of eccentric compression tests, the double symmetry of the problem allows for discretizing only one-fourth of the structure (Fig. 4). The used FE mesh consists of 27,776 hexahedral elements with trilinear displacement interpolation, 31,730 nodes, and 95,190 degrees of freedom (Fig. 4). This mesh was the result of a study regarding discretization errors. It represents a close-to-optimum trade-off between simulation effort and reliability of simulation results [23].

The simulations of the tests with the eccentricity $e = 20$ mm are based on the input values listed in Table 1. The obtained numerical results reproduce the experimental observations in a qualitatively satisfactory fashion. The rotation angle increases almost linearly with increasing load, see the black graph in Fig. 5a. However, the stiffness of the undamaged concrete hinge is overestimated by some 40%.

The simulations of the bearing capacity tests with the eccentricity $e = 25$ mm are based on the input values listed in Table 1. The obtained numerical results again reproduce the experimental observations in a qualitatively satisfactory fashion. The rotation angle increases first linearly and later superlinearly with increasing load, see the black graph in Fig. 5b. However, the initial stiffness and the bearing capacity are overestimated by some 40 and 80%, respectively.

The described quantitative differences between simulation results and experimental measurements underline that default FE input, quantified on the basis of the measured stiffness and strength of concrete, overestimates both the structural stiffness and the bearing capacity. This indicates that the concrete was damaged already before the tests.

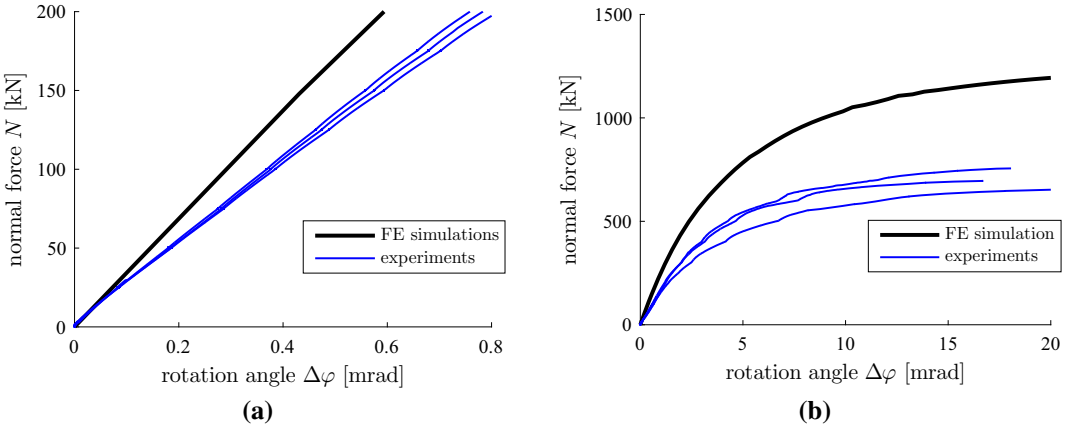

Fig. 5 Comparison of (1) numerical results from three-dimensional FE simulations, carried out using the mesh shown in Fig. 4, and based on the input values listed in Table 1 with (2) measurements from eccentric compression tests with **a** $e = 20$ mm and **b** $e = 25$ mm

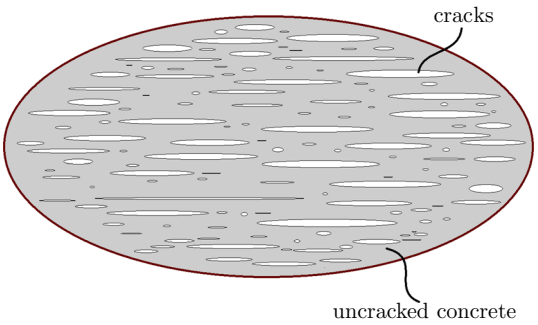

Fig. 6 Representation of damaged concrete as a matrix–inclusion composite, consisting of an uncracked concrete matrix and embedded parallel microcracks, after [19]; the two-dimensional sketch refers to a three-dimensional representative volume element

3.4 Micromechanics-assisted identification of preexisting damage of concrete

Damage may result from several possible sources, e.g., from difficulties regarding concrete placement during production of the concrete hinges. Dense reinforcement cages, limited space in the region of the narrow neck, and the three pairs of rebars crossing this region are a great challenge for placing the concrete in the formworks and to compact it thereafter. In this context, it is worth mentioning that the tested concrete hinges were produced by very experienced laboratory technicians of the research unit of the Austrian cement industry, such that highest quality standards were achieved [39]. Therefore, a more likely source of damage is shrinkage of concrete. This was already pointed out by Leonhardt for concrete hinges with reinforced necks [27], because the reinforcement cages constrain autogenous and drying shrinkage of concrete.

The available FE software allows for consideration of isotropic damage, e.g., by prescribing decreased input values of the elastic stiffness, the tensile strength, and the fracture energy. These three quantities must be identified by means of "model updating" [15], because the only available experimental data are the ones described in Sect. 2. In order to reduce the number of involved fitting parameters from three to one, it is desirable to establish correlations between the elastic stiffness, the tensile strength, and the fracture energy of concrete, on the one hand, and a corresponding damage variable on the other hand. This raises the need for a multiscale damage model for concrete.

As a first approach, a micromechanical model for failure of concrete under uniaxial tension is involved [19]. In this context, damaged concrete is idealized as a matrix–inclusion composite, consisting of a uncracked concrete matrix, which is damaged by parallel and interacting microcracks (Fig. 6). As the damage variable, the model uses the Budiansky and O'Connell crack density parameter [5,6].

Young's modulus of damaged concrete in the direction normal to the crack planes, $E_{c,\mathrm{dam}}$, decreases with increasing crack density ω. The corresponding mathematical relation follows from a Mori-Tanaka stiffness estimate [2,35,41]. It reads as [19]

$$E_{c,\mathrm{dam}} = E_c \left[1 + \frac{16\,\omega}{3}\left(1-\nu^2\right)\right]^{-1}, \tag{14}$$

where E_c, ν, and ω denote Young's modulus, Poisson's ratio of uncracked concrete, and the crack density parameter.

The tensile strength of damaged concrete, $f_{t,\mathrm{dam}}$, decreases with increasing crack density ω. The corresponding mathematical relation was derived in the framework of combined micro-fracture-mechanics approach from direct tension tests on dog-bone-shaped concrete specimens [19]. It reads as

$$f_{t,\mathrm{dam}} = \frac{0.9425\, f_t}{\sqrt{\omega + 0.8177}}. \tag{15}$$

Equations (14) and (15) establish a correlation between Young's modulus and the tensile strength of damaged concrete, by means of the damage variable ω.

The fracture energy of damaged concrete, $G_{f,\mathrm{dam}}$, decreases with increasing crack density ω. In more detail, $G_{f,\mathrm{dam}}$ is equal to the difference of the fracture energy of uncracked concrete, see G_f in Table 1, and the increment ΔG_f of the damage-related energy dissipation:

$$G_{f,\mathrm{dam}} = G_f - \Delta G_f. \tag{16}$$

In the available FE software, tensile softening is modeled on the basis of a smeared crack approach. Therefore, ΔG_f follows as the work produced by the cohesive tensile strength, σ, along the crack opening of the smeared crack, w, i.e.,

$$\Delta G_f = \int \sigma \, \mathrm{d}w. \tag{17}$$

In the available FE software the mathematical relation between σ and w is considered according to the model by Hordijk [20]. It reads as

$$\frac{\sigma}{f_t} = \left[1 + \left(c_1 \frac{w}{w_c}\right)^3\right] \exp\left(-c_2 \frac{w}{w_c}\right) - \frac{w}{w_c}\left(1 + {c_1}^3\right) \exp\left(-c_2\right), \tag{18}$$

with

$$c_1 = 3, \qquad c_2 = 6.93, \qquad w_c = 5.14\,\frac{G_f}{f_t}, \tag{19}$$

see also Fig. 7. Quantification of ΔG_f requires an expression for the crack opening displacement w as a function of the damage variable ω. To this end, Eq. (18) is specialized for Eq. (19), $\sigma = f_{t,\mathrm{dam}}$, with $f_{t,\mathrm{dam}}$ according to Eq. (15), and for numerical values of G_f and f_t, taken from Table 1. After rearranging terms, the following nonlinear expression for w_{dam} as a function of ω is obtained

$$w_{\mathrm{dam}} - 2.201 \cdot 10^{10}\, \frac{w_{\mathrm{dam}}^3 + 3.511 \cdot 10^{-13}}{\exp\left(3.274 \cdot 10^4 \cdot w_{\mathrm{dam}}\right)} = \frac{-6.989 \cdot 10^{-3}}{\sqrt{\omega + 8.177 \cdot 10^{-1}}}. \tag{20}$$

Equation (20) is solved numerically for given values of the damage variable ω. The energy, dissipated during damage-related cracking, is equal to the area under the softening curve, see the shaded area in Fig. 7b. It follows from Eqs. (17)–(20) as

$$\Delta G_f = f_t \int_0^{w_{\mathrm{dam}}} \left\{\left[1 + 27\left(\frac{w}{w_c}\right)^3\right] \exp\left(-6.93\,\frac{w}{w_c}\right) - 28\,\frac{w}{w_c}\,\exp\left(-6.93\right)\right\} \mathrm{d}w. \tag{21}$$

Preexisting damage of concrete is identified by means of correlated structural sensitivity analyses. Three different damage levels are investigated: 3, 6, and 9%. For each of these damage levels, corresponding FE input values regarding Young's modulus, the tensile strength, and the fracture energy of concrete are computed according to Eqs. (14)–(21), see also Table 2. The elastic stiffness decreases significantly with increasing damage, while the tensile strength and the fracture energy decrease only slightly. Anyway, the newly computed

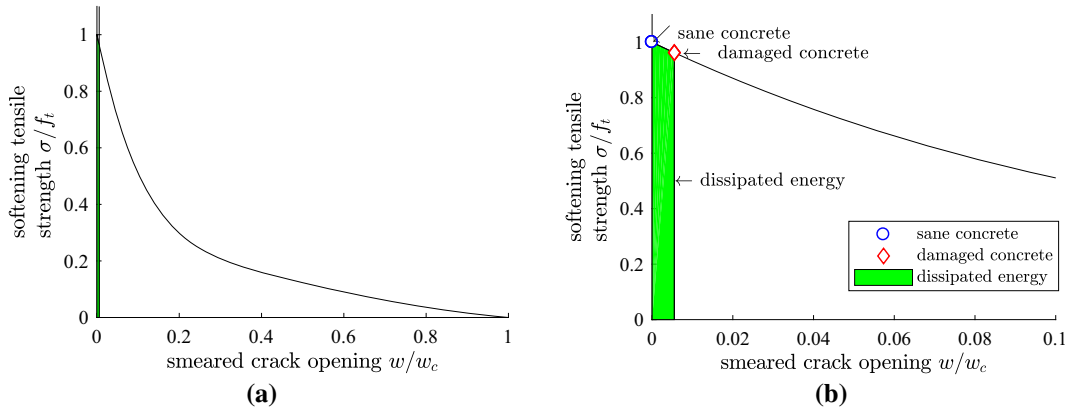

Fig. 7 Tensile softening law of the material model "CC3DNonLinCementitious2" in [9]: **a** softening tensile strength of concrete as a function of the opening displacement of a smeared crack, see also Eqs. (18) and (19) as well as Table 1; and **b** detail of the diagram shown in **a**; the shaded area is equal to the energy which was dissipated because of preexisting damage

Table 2 Input values for the concrete model "CC3DNonLinCementitious2" of Atena science [9], considering preexisting damage, based on the described micromechanics approach, see Eqs. (14)–(21)

Crack density parameter	ω	0%	3%	6%	9%	6.5%
Young's modulus	$E_{c,\mathrm{dam}}$	34,750 MPa	30,123 MPa	26,584 MPa	23,788 MPa	26,073 MPa
Uniaxial tensile strength	$f_{t,\mathrm{dam}}$	3.57 MPa	3.51 MPa	3.45 MPa	3.39 MPa	3.44 MPa
Fracture energy	$G_{f,\mathrm{dam}}$	147 J/m^2	145 J/m^2	143 J/m^2	141 J/m^2	143 J/m^2

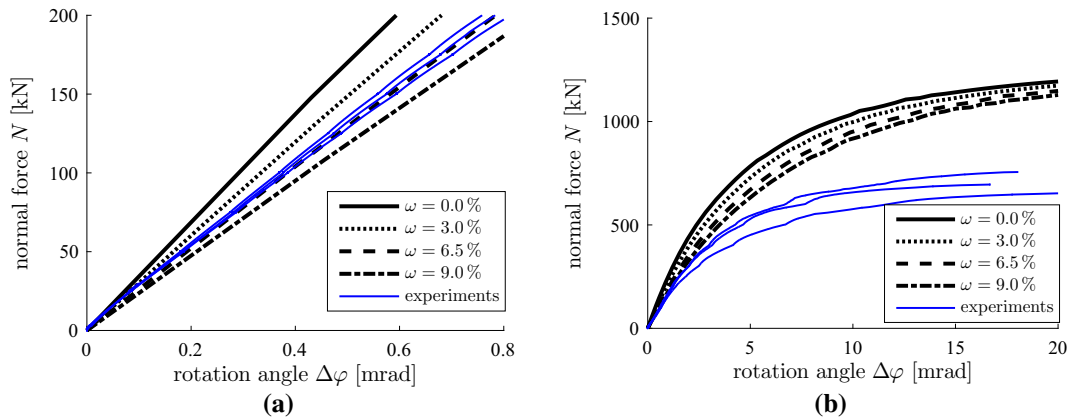

Fig. 8 Comparison of (1) numerical results from three-dimensional FE simulations, carried out using the mesh shown in Fig. 4, and based on the input values listed in Tables 1 and 2, with (2) measurements from eccentric compression tests with **a** $e = 20$ mm and **b** $e = 25$ mm

input values listed in Table 2 replace their default counterparts listed in Table 1, and the updated sets of input values are used as the basis for additional three-dimensional FE simulations. The obtained numerical results allow for assessing the sensitivity of the structural behavior of the analyzed concrete hinges with respect to preexisting damage of concrete. With increasing preexisting damage, the initial stiffness decreases significantly, see Fig. 8a, while the simulated bearing capacity decreases only slightly, see Fig. 8b. Based on interpolation, it is found that preexisting damage amounting to 6.5% allows for reproducing the experimentally observed initial stiffness of the tested concrete hinges in a qualitatively and quantitatively satisfactory fashion, see Fig 8a and the last column of Table 2.

Table 3 Triaxial-to-uniaxial compressive strength ratio, $\sigma_{\ell u}/f_c$, predicted by the Menétrey–Willam failure surface, see Eqs. (4)–(6), for the characteristic triaxial compressive stress state (13), see also Eq. (23), for input values listed in Tables 1 and 2 (see input referring to $\omega = 6.5\%$), and for different values of the auxiliary-to-actual uniaxial tensile strength ratio λ_t

λ_t	2.00	4.00	6.00	8.00	8.50
$\sigma_{\ell u}/f_c$	5.65	3.20	2.44	2.07	2.00

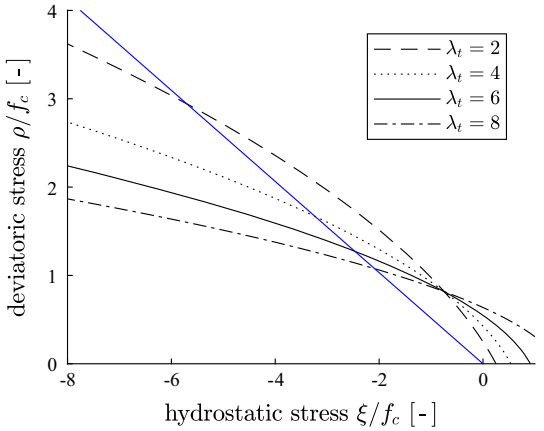

Fig. 9 Menétrey–Willam failure meridians illustrated in a section through the principal stress space containing the hydrostatic axis: Eqs. (4)–(6) evaluated for Lode angle $\vartheta = 0.84$ and input values listed in Tables 1 and 2 (see input referring to $\omega = 6.5\%$) as well as for auxiliary-to-actual uniaxial tensile strength ratios $\lambda_t \in [\,2\,,\,4\,,\,6\,,\,8\,]$; the shown meridian and the stress path (blue graph) refer to the characteristic triaxial stress state (13), see also Eq. (23)

3.5 Sensitivity analysis regarding the triaxial strength of concrete

In order to reproduce also the bearing capacity reliably, it is necessary to reduce the *triaxial* compressive strength of concrete. Notably, this modification shall neither change the uniaxial compressive strength nor the updated uniaxial tensile strength. This can be achieved by increasing the input parameter λ_t, which quantifies the ratio between the *auxiliary* uniaxial tensile strength f_t' of the Menétrey–Willam failure surface and the *actual* uniaxial tensile strength f_t of the Rankine failure surface:

$$\lambda_t = \frac{f_t'}{f_t}, \tag{22}$$

where $\lambda_t = 2$ is the corresponding default input value, see Table 1.

The starting point for the corresponding sensitivity analysis is the investigation of the characteristic triaxial compressive stress state $\boldsymbol{\sigma}$ of the investigated concrete hinges, see Eq. (13). The hydrostatic and deviatoric stress invariants as well as the Lode angle of this stress state read, according to Eqs. (7)–(9), as

$$\xi = 1.010\,\sigma_\ell, \qquad \rho = 0.521\,|\sigma_\ell|, \qquad \vartheta = 0.84. \tag{23}$$

Based on the default input parameter $\lambda_t = 2$, see Table 1, the Menétrey–Willam failure surface, see Eqs. (4)–(6), suggests that the triaxial strength $\sigma_{\ell u}$ is equal to 5.65 times the uniaxial compressive strength.

Increasing, in the framework of a sensitivity analysis, the input parameter λ_t from 2 via 4 and 6 to 8, delivers Menétrey–Willam failure surfaces with decreasing slopes in the ξ–ρ diagrams, see Fig. 9. The corresponding values of the triaxial-to-uniaxial compressive strength ratio, $\sigma_{\ell u}/f_c$, decrease from 5.65 via 3.20 and 2.44 to 2.07, see also Table 3.

As for further improved FE analyses of concrete hinges, the described modification of the Menétrey–Willam failure surface is carried out. Apart from that, default input values from Table 1 are used, except for Young's modulus, the tensile strength, and the fracture energy which are taken from the column with headline $\omega = 6.5\%$ of Table 2. Increasing the input parameter λ_t from 2 via 4 to 6 and 8, respectively, delivers simulation results, characterized by the *same* initial stiffness, but by progressively decreasing ultimate bearing capacities, see Fig. 10a. Based on extrapolation, it is found that $\lambda_t = 8.5$ allows for reproducing the experimentally obtained bearing capacity of the tested concrete hinges in a qualitatively and quantitatively

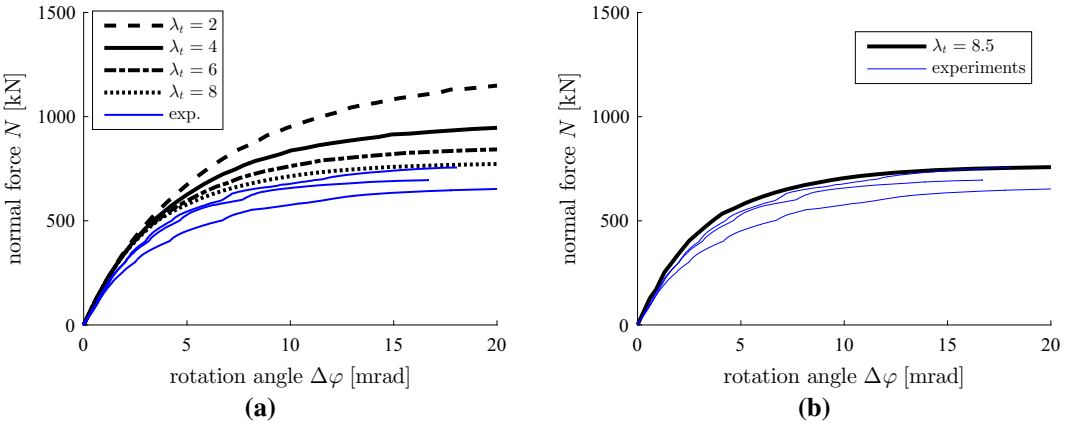

Fig. 10 Comparison of (1) numerical results from three-dimensional FE simulations, obtained using the mesh shown in Fig. 4 and based on the input values listed in Tables 1 and 2 (see input referring to $\omega = 6.5\%$) as well as different values of λ_t, with (2) measurements from eccentric compression tests with $e = 25$ mm: **a** sensitivity analysis regarding $\lambda_t \in [2, 4, 6, 8]$ and **b** simulation results obtained with an "optimum" value of $\lambda_t = 8.5$, see also Table 3

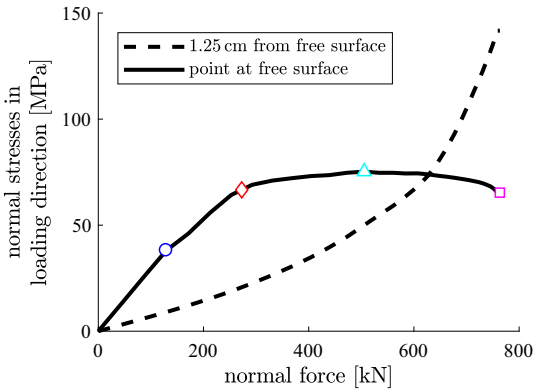

Fig. 11 Simulated normal stresses in loading direction as a function of the eccentric normal force; comparison of a point at the free surface of the notch root (see the solid line) with a point inside the concrete hinge, in a distance of 1.25 cm from the free surface (see the dashed line)

satisfactory fashion, see Fig 10b. Notably, $\lambda_t = 8.5$ refers to a triaxial-to-uniaxial compressive strength ratio amounting to 2, see the last column of Table 3.

The ductile *structural* failure of concrete hinges results from the ductile *material* failure of concrete at the innermost *surface* of the compressed lateral notch, where a biaxial compressive stress state prevails. This is underlined by the evolution of normal stresses in loading direction as a function of the eccentric normal force, see Fig. 11. The normal stress in loading direction at the free surface of the notch root increases linearly with increasing loading up to 130 kN, see the circle in Fig. 11, which defines the elastic limit. It is followed by virtually linear hardening up to 270 kN, see the rhombus in Fig. 11, and very moderate continued hardening up to 510 kN, see the triangle in Fig. 11. Subsequently, the normal stress component decreases slightly, indicating material softening up to the bearing capacity of 763 kN, see the square in Fig. 11. Interestingly, the normal stress in loading direction *inside* the concrete hinge, in a distance of 1.25 cm from the free surface increases monotonously and superlinearly with increasing eccentric normal force, see Fig. 11. This is a result of the confinement-induced strengthening of concrete.

4 Interaction envelopes for concrete hinges subjected to compression and bending

In the following, it is shown that the triaxial-to-uniaxial compressive strength ratio $\sigma_{\ell u}/f_c = 2$ is consistent with Eurocode 2, when applying regulations for partially loaded areas to the investigated concrete hinges. As

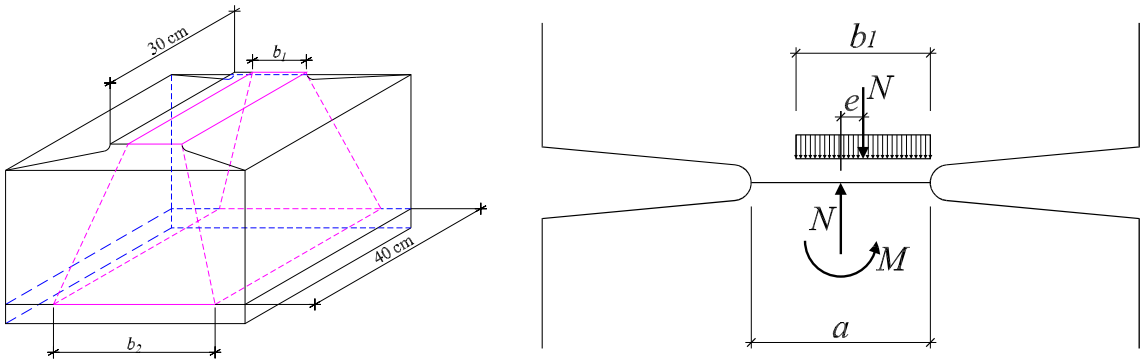

(a) **(b)**

Fig. 12 Application of the regulations of Eurocode 2 regarding partially loaded areas [4] to concrete hinges: **a** geometric dimensions, and **b** stress distribution in the uncracked ligament of the neck

for a partially loaded area (Fig. 12), Eurocode 2 allows a maximum compressive force F_{Rdu} which reads as [4]

$$F_{Rdu} = A_{co}\, f_{cd} \sqrt{\frac{A_{c1}}{A_{c0}}}, \tag{24}$$

where $A_{c0} = d_1\, b_1$ is the loaded area, f_{cd} denotes the uniaxial compressive strength, and $A_{c1} = d_2\, b_2$ stands for the "maximum distribution area with a similar shape to A_{c0}" [4]. Eq. (24) suggests that the triaxial-to-uniaxial strength ratio amounts to $\sqrt{A_{c1}/A_{c0}}$.

Applying Eq. (24) to the herein investigated concrete hinges, A_{c0} is equal to the uncracked area of the neck, such that $d_1 = 30\,\text{cm}$ is the length of the neck in the thickness direction, b_1 is the length of the uncracked neck ligament in the lateral direction, see Fig. 12a, $d_2 = 40\,\text{cm}$ is the length of the concrete hinge in the thickness direction, and $b_2 = 3\, b_1$ [4]. Specifying the triaxial-to-uniaxial compressive strength ratio for these geometric properties, delivers

$$\sqrt{\frac{A_{c1}}{A_{c0}}} = \sqrt{\frac{3\, b_1 \cdot 40}{b_1 \cdot 30}} = 2. \tag{25}$$

Interestingly, this is equal to the triaxial-to-uniaxial compressive strength ratio which was identified in Sect. 3, see the last column of Table 3.

In order to derive a Eurocode-inspired interaction envelope for concrete hinges subjected to compression and bending, the length b_1 of the uncracked neck ligament is used as a parameter. Considering that compressive normal stresses in the loading direction, amounting to $2\, f_c$, prevail along the uncracked ligament b_1 of concrete, see Fig. 12b, the resulting normal force reads as

$$N = 2\, f_c\, b_1\, d_1. \tag{26}$$

This normal force has an eccentricity $e = (a - b_1)\,/2$ with respect to the midplane of the concrete hinge, see Fig. 12b. Therefore, the resulting bending moment reads as [43]

$$M = N\, \frac{a - b_1}{2} = f_c\, b_1\, d_1\, (a - b_1). \tag{27}$$

The interaction envelope is obtained by solving Eq. (26) for the parameter b_1 and using the resulting expression to eliminate the parameter b_1 from Eq. (27):

$$M = \frac{N}{2} \left(a - \frac{N}{2\, f_c\, d_1} \right), \tag{28}$$

where $a = 75\,\text{mm}$, $f_c = 49\,\text{MPa}$, and $d_1 = 300\,\text{mm}$. The failure envelope (28) agrees very well with the experimentally determined bearing capacities for eccentric compression, see Fig. 13.

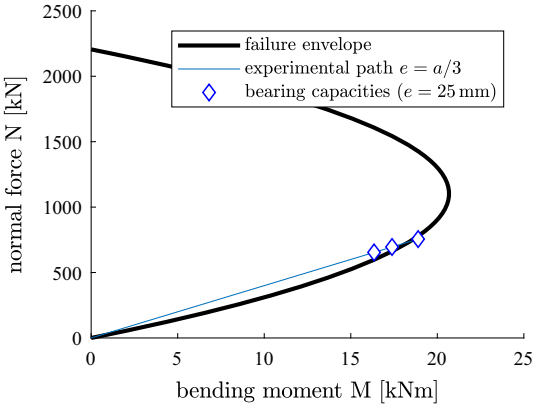

Fig. 13 Eurocode-inspired failure envelope for concrete hinges subjected to compression and bending according to Eq. (28) and comparison with the bearing capacity tests reported in [39], see also Fig. 2b

5 Discussion

The bearing capacity of concrete hinges subjected to eccentric compression was re-analyzed by means of three-dimensional FE analyses. Numerical results provide insight into the functionality of concrete hinges. The following discussion focuses (1) on the triaxial stress states prevailing in the compressed part of the neck region and (2) on the mechanisms that enable a failure of concrete hinges in the experimentally observed ductile fashion.

FE simulations allowed for quantifying the *triaxial* compressive stress states prevailing in the neck region of the analyzed concrete hinges. Notably, the compressive normal stresses in the lateral and the thickness directions result from stress trajectories that must run around the notches. The inclination angles of the stress trajectories create the desired compressive stresses, orthogonal to the loading direction. While this underlines the importance of front-side notches, it is also interesting to note that the characteristic principal compressive stress ratio was quantified as 1.00 : 0.45 : 0.30. Such a pronounced stress triaxiality implies the existence of an isotropic stress part which amounts to almost 60% of the principal stress acting in loading direction. This confinement pressure results in a considerable increase of the strength of concrete relative to its uniaxial compressive strength. Superficially, this explains the impressive bearing capacity of concrete hinges. In more depth, however, it is important to realize that a three-axial stress state is impossible at the free surface in the innermost region of the compressed lateral neck, because of the traction-free boundary condition prevailing at this neck root.

A *plane* stress state prevails at the air-exposed neck root. In this context, it is noteworthy that the biaxial compressive strength of concrete is only a few percent larger than the uniaxial compressive strength of the material [25]. Consequently, the strength of concrete at the surface of the neck root is reached already at external load intensities that are significantly smaller than the bearing capacity of the concrete hinge. Still, both the experiments and the numerical simulations show that there is no spalling of the failing surface layer at the neck root. More importantly, the stress state does not decrease significantly, see Fig. 11, although the strains do increase considerably. In other words, the surface layer exhibits a *ductile* rather than a brittle failure behavior. The continued integrity of the surface layer at the neck root, in turn, is essential for the built-up of the triaxial compressive stress state *behind* the surface layer. If the surface layer would spall away, the neighboring layer, which initially was *inside* the volume of the structure, would become the new surface layer. Consequently, the initially triaxial stress state would transform all over sudden into a biaxial stress state such that the strength of the material would drop from the large strength under confined triaxial compression to the much smaller strength under biaxial compression. This renders it likely that initiation of spalling at the surface of the neck root would result in a catastrophic domino effect. A spalling front would propagate quickly in the direction toward the center of the concrete hinge. Anyway, there is plenty of evidence from testing of concrete hinges and from practical applications that spalling does not take place as long as the loading is not close to the bearing capacity of the concrete hinges. This underlines that the ductile failure behavior of concrete under biaxial compression at the surface of the neck root is the mechanism which makes it possible that concrete hinges fail in the experimentally observed ductile fashion.

6 Conclusions

Testing provides very valuable insight into the structural performance of concrete hinges. However, available deformation and displacement measurements are typically limited to the easily accessible surface of concrete hinges. In order to gain insight into what is happening inside the volume of concrete hinges, FE simulations are indispensable. Herein, they allowed for quantifying the *triaxial* compressive stress states prevailing in the neck region and the mechanism which makes it possible for concrete hinges to fail in a ductile fashion. From the presented study, the following conclusions are drawn:

- As for the investigated concrete hinges, the triaxial compressive stress state in the neck region exhibits a characteristic ratio of the principal stresses in the loading direction, the thickness direction, and the lateral direction, amounting to 1.00 : 0.45 : 0.30.
- This stress triaxiality is a consequence of the notches, because the stress trajectories must run around them. The inclination angles of the stress trajectories create the desired compressive stresses, orthogonal to the loading direction. This underlines the importance of front-side notches.
- The ratio of principal compressive stresses, 1.00 : 0.45 : 0.30, implies that the isotropic part of the stress state amounts to almost 60% of the compressive stresses in the loading direction. This significant confinement pressure results in a considerable strengthening of the concrete, relative to its uniaxial compressive strength.
- Herein, the strengthening factor was identified to amount to 2. This is consistent with Eurocode regulations for partially loaded areas of concrete.
- Quantifying the triaxial strength of concrete on the basis of Eurocode regulations for *partially loaded areas* allows for (1) simulating realistic bearing capacities of concrete hinges in the context of numerical multiscale structural analysis, and (2) deriving reasonable failure envelopes for concrete hinges subjected to compression and bending.
- The ductile *structural* failure mode of concrete hinges results from the ductile *material* failure of concrete at the innermost surface of the compressed lateral notch, where a *biaxial compressive* stress state prevails. This ductile material failure enables (1) the built-up of triaxial stress states inside the volume of concrete hinges, and (2) remarkably large bearing capacities of concrete hinges subjected to compression and bending.

Acknowledgements Open access funding provided by Austrian Science Fund (FWF). Financial support by the Austrian Ministry for Transport and Technology (bmvit), the Austrian Research Promotion Agency (FFG), ÖBB-Infrastruktur AG, ASFINAG Bau Management GmbH, provided within the VIF-project 845681 “Optimierte Bemessungsregeln für dauerhafte bewehrte Betongelenke” and corresponding discussions with Michael Schweigler (TU Wien), Susanne Gmainer and Martin Peyerl (Smart Minerals GmbH), Alfred Hüngsberg (ÖBB-Infrastruktur AG), Erwin Pilch and Michael Kleiser (ASFINAG Bau Management GmbH) are gratefully acknowledged. Additional interesting discussions regarding the use of concrete hinges in mechanized tunneling, carried out within the Austrian Science Fund (FWF) project P 281 31-N32 “Bridging the Gap by means of Multiscale Structural Analysis” with Yong Yuan (Tongji University) and Jiaolong Zhang (TU Wien/Tongji University) are also gratefully acknowledged.

Compliance with ethical standards

Conflict of interest The authors declare that they have no conflict of interest.

References

1. Austrian Standards Institute: ONR 23303:2010-09-01 Prüfverfahren Beton (PVB)—Nationale Anwendung der Prüfnormen für Beton und seiner Ausgangsstoffe [Test protocol concrete - National application of testing standards for concrete and its raw materials], vol. ONR 23303. Austrian Standards Institute (2010) (in German)
2. Benveniste, Y.: A new approach to the application of Mori–Tanaka’s theory in composite materials. Mech. Mater. **6**(2), 147–157 (1987). https://doi.org/10.1016/0167-6636(87)90005-6
3. Blom, C.B.M.: Design philosophy of concrete linings for tunnels in soft soils. Doctoral dissertation, Delft University of Technology (2002)
4. British Standards Institution, CEN European Committee for Standardization: EN 1992-1-1:2015-07-31 Eurocode 2: design of concrete structures—part 1-1: general rules and rules for buildings (2015)
5. Budiansky, B.: On the elastic moduli of some heterogeneous materials. J. Mech. Phys. Solids **13**(4), 223–227 (1965). https://doi.org/10.1016/0022-5096(65)90011-6

6. Budiansky, B., O'Connell, R.J.: Elastic moduli of a cracked solid. Int. J. Solids Struct. **12**(2), 81–97 (1976). https://doi.org/10.1016/0020-7683(76)90044-5
7. Červenka, J., Papanikolaou, V.K.: Three dimensional combined fracture-plastic material model for concrete. Int. J. Plast. **24**(12), 2192–2220 (2008). https://doi.org/10.1016/j.ijplas.2008.01.004
8. Červenka, V., Jendele, L., Červenka, J.: ATENA program documentation part 1—theory, February 5, 2016 edn. http://www.cervenka.cz/assets/files/atena-pdf/ATENA_Theory.pdf (2016)
9. Cervenka Consulting, Červenka, V., Jendele, L., Červenka, J., et al.: Build 12562 & ATENA 5.1.3. Internet source. http://www.cervenka.cz/download/#atena-gid (2016)
10. Chen, J., Mo, H.: Numerical study on crack problems in segments of shield tunnel using finite element method. Tunn. Undergr. Space Technol. **24**(1), 91–102 (2009). https://doi.org/10.1016/j.tust.2008.05.007
11. De Waal, R.G.A.: Steel fibre reinforced tunnel segments: for the application in shield driven tunnel linings. Doctoral dissertation, Delft University of Technology (2000)
12. fib: fib Model Code for Concrete Structures 2010. Ernst & Sohn, Wiley (2013). https://doi.org/10.1002/9783433604090
13. Freyssinet, E.: Le pont de Candelier [The bridge of Candelier]. Ann. Ponts Chaussées **1**, 165f (1923)
14. Freyssinet, E.: Naissance du béton précontraint et vues d'avenir [Birth of prestressed concrete and future outlook]. Travaux, pp. 463–474 (1954)
15. Friswell, M.I., Mottershead, J.E.: Finite Element model updating in structural dynamics, vol. 38. Springer (1995). https://doi.org/10.1007/978-94-015-8508-8
16. Gladwell, G.M.: Contact problems in the classical theory of elasticity. Springer (1980). https://doi.org/10.1007/978-94-009-9127-9
17. Grassl, P., Jirásek, M.: Damage-plastic model for concrete failure. Int. J. Solids Struct. **43**(2223), 7166–7196 (2006). https://doi.org/10.1016/j.ijsolstr.2006.06.032
18. Hefny, A.M., Chua, H.C.: An investigation into the behaviour of jointed tunnel lining. Tunn. Underg. Space Technol. **21**(34), 428 (2006). https://doi.org/10.1016/j.tust.2005.12.070. In: Safety in the Underground Space—Proceedings of the ITA-AITES 2006 World Tunnel Congress and 32nd ITA General Assembly
19. Hlobil, M., Göstl, M., Burrus, J., Hellmich, C., Pichler, B.: Molecular-to-macro upscaling of concrete fracture: theory and experiments. J. Mech. Phys. Solids, under revision (2017)
20. Hordijk, D.A.: Local Approach to Fatigue of Concrete, vol. 210. Doctoral dissertation, Delft University of Technology, The Netherlands (1991). ISBN 90/9004519-8
21. Janßen, P.: Tragverhalten von Tunnelausbauten mit Gelenkstübbings [Structural behavior of segmented tunnel linings]. Ph.D. thesis, Technical University of Braunschweig (1986)
22. Jusoh, S.N., Mohamad, H., Marto, A., Yunus, N.Z.M., Kasim, F.: Segment's joint in precast tunnel lining design. J. Teknol. **77**(11), 91–98 (2015). https://doi.org/10.11113/jt.v77.6426
23. Kalliauer, J.: Insight into the structural behavior of concrete hinges by means of finite element simulations. Master thesis, TU Wien, Karslplatz 13, 1010 Wien (2016)
24. Klappers, C., Grübl, F., Ostermeier, B.: Structural analyses of segmental lining—coupled beam and spring analyses versus 3D-FEM calculations with shell elements. Tunn. Undergr. Space Technol. **21**(3–4), 254–255 (2006). https://doi.org/10.1016/j.tust.2005.12.116
25. Kupfer, H., Hilsdorf, H.K., Rusch, H.: Behavior of concrete under biaxial stresses. J. Proc. **66**(8), 656–666 (1969)
26. Leonhardt, F.: Mainbrücke Gemünden—Eisenbahnbrücke aus Spannbeton mit 135 m Spannweite [Bridge over the river Main at Gemünden—prestressed railway bridge with a span of 135 m]. Beton Stahlbetonbau **81**(1), 1–8 (1986). https://doi.org/10.1002/best.198600010
27. Leonhardt, F., Reimann, H.: Betongelenke: Versuchsbericht, Vorschläge zur Bemessung und konstruktiven Ausbildung. Kritische Spannungszustände des Betons bei mehrachsiger, ruhender Kurzzeitbelastung [Concrete hinges: test report, recommendations for structural design. Critical stress states of concrete under multiaxial static short-term loading], vol. 175. Ernst und Sohn, Berlin (1965) (in German)
28. Maidl, B., Herrenknecht, M., Maidl, U., Wehrmeyer, G.: Mechanised Shield Tunnelling. Wiley-Blackwell (2012). https://doi.org/10.1002/9783433601051
29. Majdi, A., Ajamzadeh, H., Nadimi, S.: Investigation of moment–rotation relation in different joint types and evaluation of their effects on segmental tunnel lining. Arab. J. Geosci. **9**(7), 1–15 (2016). https://doi.org/10.1007/s12517-016-2538-z
30. Marx, S., Schacht, G.: Betongelenke im Brückenbau [Concrete hinges in bridge construction], vol. 18. Deutscher Beton- und Bautechnik-Verein e.v. (2010) (in German)
31. Marx, S., Schacht, G.: Concrete hinges—historical development and contemporary use. 3rd *fib* International Congress, 2010, pp. 1–21 (2010)
32. Marx, S., Schacht, G.: Gelenke im Massivbau [Hinges in concrete structures]. Beton Stahlbetonbau **105**(1), 27–35 (2010). https://doi.org/10.1002/best.200900061. (in German)
33. Menétrey, P., Willam, K.J.: Triaxial failure criterion for concrete and its generalization. ACI Struct. J. **92**(3), 311–318 (1995). https://doi.org/10.14359/1132
34. Morgenthal, G., Olney, P.: Concrete hinges and integral bridge piers. J. Bridge Eng. **21**(1), 06015,005 (2016). https://doi.org/10.1061/(ASCE)BE.1943-5592.0000783
35. Mori, T., Tanaka, K.: Average stress in matrix and average elastic energy of materials with misfitting inclusions. Acta Metall. **21**(5), 571–574 (1973). https://doi.org/10.1016/0001-6160(73)90064-3
36. Sallenbach, H.H: Betongelenke beim Hardturm-Viadukt [Concrete hinges for the Hardturm-Viadukt]. Schweizer Bauzeitung **85** (1967)
37. Schacht, G., Marx, S.: Unbewehrte Betongelenke—100 Jahre Erfahrung im Brückenbau [Unreinforced concrete hinges—100 years of experience in bridge construction]. Beton Stahlbetonbau **105**(9), 599–607 (2010). (in German)
38. Schacht, G., Marx, S.: Concrete hinges in bridge engineering. Proc. Inst. Civ. Eng. Eng. Hist. Herit. **168**(2), 65–75 (2015). https://doi.org/10.1680/ehah.14.00020

39. Schlappal, T., Schweigler, M., Gmainer, S., Peyerl, M., Pichler, B.: Creep and cracking of concrete hinges: insight from centric and eccentric compression experiments. Mater. Struct. **50**(6), 244 (2017). https://doi.org/10.1617/s11527-017-1112-9
40. Teachavorasinskun, S., Chub-uppakarn, T.: Influence of segmental joints on tunnel lining. Tunn. Undergr. Space Technol. **25**(4), 490–494 (2010). https://doi.org/10.1016/j.tust.2010.02.003
41. Zaoui, A.: Continuum micromechanics: survey. J. Eng. Mech. **128**(8), 808–816 (2002). https://doi.org/10.1061/(asce)0733-9399(2002)128:8(808)
42. Zhang, W., Jin, X., Yang, Z.: Combined equivalent & multi-scale simulation method for 3-D seismic analysis of large-scale shield tunnel. Eng. Comput. **31**(3), 584–620 (2014). https://doi.org/10.1108/EC-02-2012-0034
43. Ziegler, F.: Mechanics of solids and fluids, 2nd edn. Springer (1995). https://doi.org/10.1007/978-1-4612-0805-1